Absence of electron transfer-associated changes in the time-dependent X-ray free-electron laser structures of the photosynthetic reaction center

Gai Nishikawa [1], Yu Sugo [1], Keisuke Saito [1,2], and Hiroshi Ishikita [1,2]*

1) Department of Applied Chemistry, The University of Tokyo, 7-3-1 Hongo, Bunkyo-ku, Tokyo 113-8654, Japan

2) Research Center for Advanced Science and Technology, The University of Tokyo, 4-6-1 Komaba, Meguro-ku, Tokyo 153-8904, Japan

CORRESPONDING AUTHOR: Ishikita, Research Center for Advanced Science and Technology, The University of Tokyo, 4-6-1 Komaba, Meguro-ku, Tokyo 153-8904, Japan, Tel. +81-3-5452-5056, Fax. +81-3-5452-5083, **E-mail:** hiro@appchem.t.u-tokyo.ac.jp

ABSTRACT

Using the X-ray free-electron laser (XFEL) structures of the photosynthetic reaction center from *Blastochloris viridis* that show light-induced time-dependent structural changes [Dods, R.et al. (2021) Nature *589*, 310-314], we investigated time-dependent changes in the energetics of the electron transfer pathway, considering the entire protein environment of the protein structures and titrating the redox active sites in the presence of all fully equilibrated titratable residues. In the dark and charge-separation intermediate structures, the calculated redox potential (E_m) values for the accessory bacteriochlorophyll and bacteriopheophytin in the electron-transfer active branch (B_L and H_L) are higher than those in the electron-transfer inactive branch (B_M and H_M). However, the stabilization of the $[P_LP_M]^{\bullet+}H_L^{\bullet-}$ state owing to protein reorganization is not clearly observed in the $E_m(H_L)$ values in the charge-separated 5-ps ($[P_LP_M]^{\bullet+}H_L^{\bullet-}$ state) structure. Furthermore, the expected chlorin ring deformation upon formation of $H_L^{\bullet-}$ (saddling mode) is absent in the H_L geometry of the original 5-ps structure. These findings suggest that there is no clear link between the time-dependent structural changes and the electron transfer events in the XFEL structures.

31 **INTRODUCTION**

32 Photosynthetic reaction centers from purple bacteria (PbRC) are heterodimeric reaction centers, which
33 are formed by the protein subunits L and M (Figure 1). In PbRC from *Blastochloris viridis*, the electronic
34 excitation of the bacteriochlorophyll *b* (BChl*b*) pair, $[P_LP_M]$, leads to electron transfer to accessory BChl*b*,
35 B_L, followed by electron transfer via bacteriopheophytin *b* (BPheo*b*), H_L, to menaquinone, Q_A, along the
36 electron-transfer active L branch (A branch) (*1*). Electron transfer further proceeds from Q_A to ubiquinone,
37 Q_B, which is coupled with proton transfer via charged and polar residues in the Q_B binding region (*2*).
38 Although the counterpart M branch (B branch) is essentially electron-transfer inactive, mutations of the
39 Phe-L181/Tyr-M208 pair to tyrosine/phenylalanine lead to an increase in the yield of $[P_LP_M]^{\bullet+}H_M^{\bullet-}$
40 formation (~30%), which suggests that these residues are responsible for the energetic asymmetry in the
41 electron transfer branches (e.g., (*3*)). The anionic states $B_L^{\bullet-}$, $H_L^{\bullet-}$, and $Q_A^{\bullet-}$ form in ~3.5 ps, ~5 ps, and
42 ~200 ps upon the formation of the electronically excited $[P_LP_M]^*$ state, respectively (*4*). The anionic state
43 formation induces not only reoriganization of the protein environment (*5*) but also out-of-plane distortion
44 of the chlorin ring (*6*). Indeed, two distinct conformations of $H_L^{\bullet-}$ were reported in spectroscopic studies
45 of PbRC from *Rhodobacter sphaeroides* (*7*).

46 Recently, using the X-ray free electron laser (XFEL), light-induced electron density changes and
47 structural changes of PbRC were analyzed at 1 ps, 5 ps, 20 ps, 300 ps, and 8 μs upon the electronic
48 excitation of $[P_LP_M]$ at 960 nm (*8*): the 1 ps XFEL structure represents the $[P_LP_M]^*$ state, the 5 ps and 20
49 ps XFEL structures represent the charge-separated $[P_LP_M]^{\bullet+}H_L^{\bullet-}$ state, and the 300 ps and 8 μs XFEL
50 structures represent the charge-separated $[P_LP_M]^{\bullet+}Q_A^{\bullet-}$ state. According to Dods et al. (*8*), these XFEL
51 structures revealed how the charge-separation process was stabilized by protein conformational dynamics.
52 However, the conclusion was drawn from the XFEL structures, of which 8 out of 9 are at a resolution of
53 2.8 Å (atomic coordinates from PDB codes: 5O4C, 6ZI4, and 6ZI5 for dataset a and 6ZHW, 6ZID, 6ZI6,
54 6ZI9, and 6ZIA for dataset b) (*8*).

55

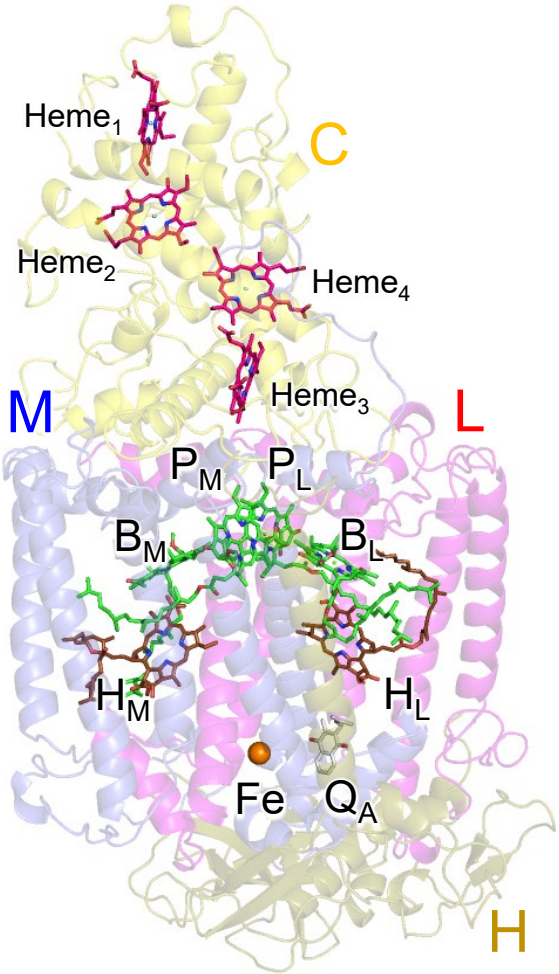

Figure 1. Locations of redox-active cofactors in PbRC from *Blastochloris viridis*.

Here, we investigated how the redox potential (E_m) values of the BChl*b* and BPheo*b* cofactors for one-electron reduction change as electron transfer proceeds using the dark (0 ps), 1 ps, 5 ps, 20 ps, 300 ps, and 8 μs XFEL structures, solving the linear Poisson-Boltzmann equation, and considering the protonation states of all titratable sites in the entire protein. Structural changes (e.g., side-chain orientation) in the protein environment can be analyzed in the E_m shift, as E_m is predominantly determined by the sum of the electrostatic interactions between the redox-active site and all other groups (i.e., residues and cofactors) in the protein structure. Subtle structural changes of the BChl*b* and BPheo*b* chlorin rings, which may not be pronounced even in the E_m shift (*6*), can be analyzed in the out-of-plane distortion of the chlorin rings

using a normal-coordinate structural decomposition (NSD) analysis (*9, 10*) with a combination of a quantum mechanical/molecular mechanical (QM/MM) approach in the entire PbRC protein environment.

METHODS

Coordinates and atomic partial charges. The atomic coordinates of PbRC from *Blastochloris viridis* were taken from the XFEL structures determined at 0 ps (dark state; PDB code 5O4C for dataset a and 5NJ4 for dataset b), 1 ps ($[P_LP_M]^*$ state; PDB code, 6ZHW for dataset b), 5 ps ($[P_LP_M]^{\bullet+}H_L^{\bullet-}$ state; PDB code, 6ZI4 for dataset a and 6ZID for dataset b), 20 ps ($[P_LP_M]^{\bullet+}H_L^{\bullet-}$ state; PDB code, 6ZI6 for dataset b), 300 ps ($[P_LP_M]^{\bullet+}Q_A^{\bullet-}$ state; PDB code, 6ZI5 for dataset a and 6ZI9 for dataset b), and 8 μs ($[P_LP_M]^{\bullet+}Q_A^{\bullet-}$ state; PDB code, 6ZIA for dataset b). Atoms with 30% occupancy for the photoactivated state (*8*) were used wherever present. Hydrogen atoms were generated and energetically optimized with CHARMM (*11*). Atomic partial charges of the amino acids were adopted from the all-atom CHARMM22 (*12*) parameter set. The atomic charges of diacylglycerol, the Fe complex (*13*), and menaquinone (*14*)) were obtained from previous studies. The atomic charges of BChl*b* and BPheo*b* (BChl*b*, BChl$b^{\bullet+}$, BChl$b^{\bullet-}$, BPheo*b*, and BPheo$b^{\bullet-}$) were determined by fitting the electrostatic potential in the neighborhood of these molecules using the RESP procedure (*15*) (Tables S1). The electronic densities were calculated after geometry optimization by the DFT method with the B3LYP functional and 6-31G** basis sets using the JAGUAR program (*16*). For the atomic charges of the nonpolar CH_n groups in cofactors (e.g., the phytol chains of BChl*b* and BPheo*b* and the isoprene side chains of quinones), the value of +0.09 was assigned for nonpolar H atoms.

***E*m calculation: solving the linear Poisson-Boltzmann equation.** To obtain the E_m values in the proteins, we calculated the electrostatic energy difference between the two redox states in a reference model system by solving the linear Poisson-Boltzmann equation with the MEAD program (*17*) and using E_m(BChl*b*) = –665 mV and E_m(BPheo*b*) = –429 mV (based on E_m(BChl*b*) = –700 mV and E_m(BPheo*b*) = –500 mV for one-electron reduction measured in dimethylformamide (*18, 19*)), considering the

92 solvation energy difference). The difference in the E_m value of the protein relative to the reference system
93 was added to the known E_m value. The ensemble of protonation patterns was sampled by the Monte Carlo
94 method with Karlsberg (*20*). The linear Poisson-Boltzmann equation was solved using a three-step grid-
95 focusing procedure at resolutions of 2.5 Å, 1.0 Å, and 0.3 Å. Monte Carlo sampling yielded the
96 probabilities $[A_{ox}]$ and $[A_{red}]$ of the two redox states of molecule *A*. E_m was evaluated using the Nernst
97 equation. A bias potential was applied to obtain an equal amount of both redox states ($[A_{ox}] = [A_{red}]$),
98 thereby yielding the redox midpoint potential as the resulting bias potential. To facilitate direct
99 comparisons with previous computational results (e.g., (*13*)), identical computational conditions and
100 parameters were used; all computations were performed at 300 K, pH 7.0, and an ionic strength of 100
101 mM. The dielectric constants were set to 4 for the protein interior and 80 for water.

102 **QM/MM calculations.** We employed the restricted DFT method for describing the closed-shell
103 electronic structure and the unrestricted DFT method for the open-shell electronic structure with the
104 B3LYP functional and LACVP* basis sets using the QSite (*21*) program. Counter ions were added to
105 neutralize the entire system. In the QM region, all atom positions were relaxed in the QM region, while
106 the H-atom positions were relaxed in the MM region. The QM regions were defined as follows: for the
107 BChl*b* pair [P_LP_M]: the side chains of the ligand residues (His-L173 and His-M200) and H-bod partners
108 (His-L168, Tyr-M195, and Thr-L248); for accessory BChl*b*: B_L/B_M and the side chain of the ligand
109 residue (His-L153 for B_L/His-M180 for B_M); for BPheo*b*: H_L/H_M.

110 **NSD analysis.** To analyze the out-of-plane distortions of chlorin rings, we employed an NSD procedure
111 with the minimal basis approximation, where the deformation profile can be represented by the six lowest-
112 frequency normal modes, i.e., ruffling (B_{1u}), saddling (B_{2u}), doming (A_{2u}), waving ($E_{g(x)}$ and $E_{g(y)}$), and
113 propellering (A_{1u}) modes (*9, 10*). The NSD analysis was performed in the following three steps, as
114 performed previously (*6*). First, the atomic coordinates of the Mg-substituted macrocycle were extracted
115 from the crystal (or QM/MM optimized) structure. Second, the extracted coordinates were superimposed
116 on the reference coordinates of the macrocycle. The superimposition is based on a least-square method,

and the mathematical procedure is described in Ref. (*22*). Finally, the out-of-plane distortion in the superimposed coordinates was decomposed into the six lowest-frequency normal modes by the projection to the reference normal mode coordinates as

$$d^{\Gamma} = \sum_{i=1}^{N} \Delta z_i (n_z^{\Gamma})_i \,, \qquad \text{(Eq.1)}$$

where d^{Γ} represents the distortion component of the mode Γ (i.e., Γ = B_{1u}, B_{2u}, A_{2u}, $E_{g(x)}$, $E_{g(y)}$, or A_{1u}), Δz_i is the *z*-component of the superimposed coordinates in the *i*th heavy atom, and $(n_z^{\Gamma})_i$ is the *z*-component of the normalized eigenvector of the reference normal mode Γ in the *i*th heavy atom. *N* represents the number of heavy atoms. See ref. (*6*) for further details.

RESULTS AND DISCUSSION

Energetically asymmetric electron transfer branches. The XFEL structures show that the E_m values for B_L are ~50 mV higher than those for B_M, which facilitates the formation of the charge-separated $[P_LP_M]^{\bullet+}B_L^{\bullet-}$ state and thereby electron transfer along the L-branch (Figures 2 and 3). As the E_m profile is substantially consistent with the E_m profile for PbRC from *Rhodobacter sphaeroides* (*13*), it seems plausible that the charge-separated $[P_LP_M]^{\bullet+}B_L^{\bullet-}$ and $[P_LP_M]^{\bullet+}H_L^{\bullet-}$ states in the active L-branch are energetically lower than the $[P_LP_M]^{\bullet+}B_M^{\bullet-}$ and $[P_LP_M]^{\bullet+}H_M^{\bullet-}$ states in the inactive M-branch, respectively, as demonstrated in QM/MM/PCM calculations (*23*). Indeed, the calculated E_m values are largely correlated with the LUMO levels calculated using a QM/MM approach, as suggested previously (coefficient of determination R^2 = 0.98, Figure S1). The $E_m(H_L)$ value of –597 mV is in line with the experimentally estimated value of ca. –600 mV for H_L in PbRC from *Blastochloris viridis* (*24*).

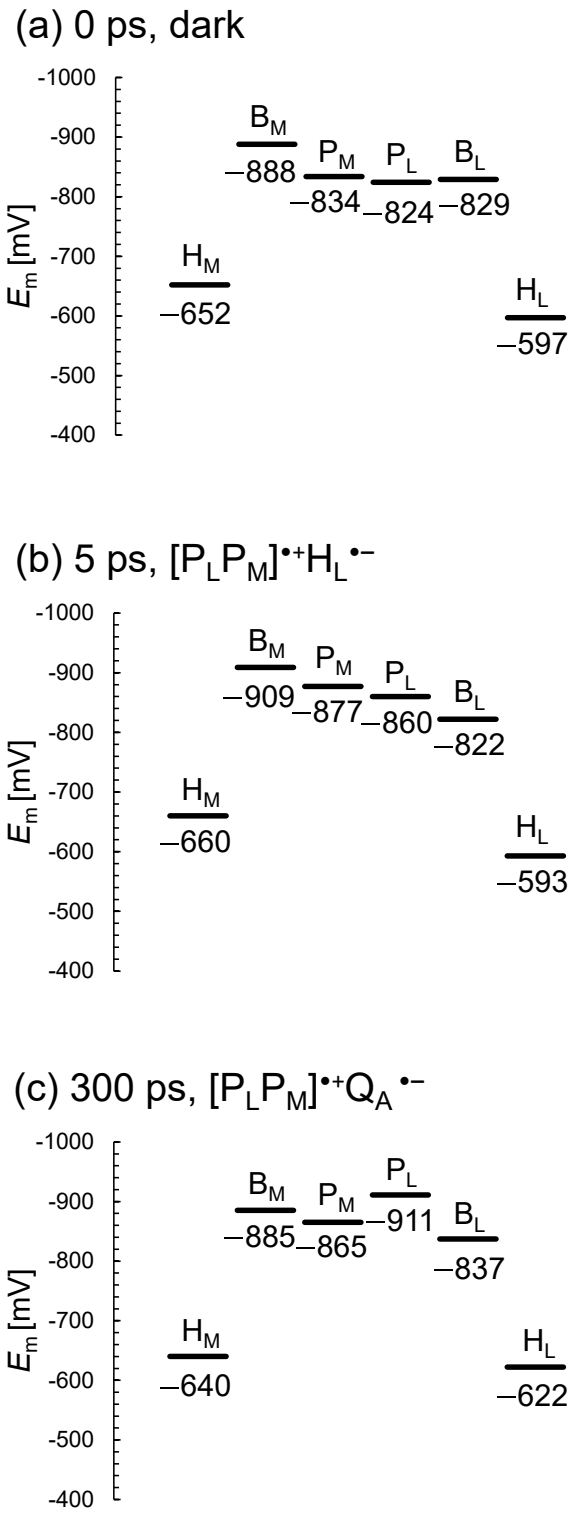

Figure 2. E_m profiles along the L- and M-branches in the XFEL structures for dataset a. (a) 0 ps. (b) 5 ps. (c) 300 ps.

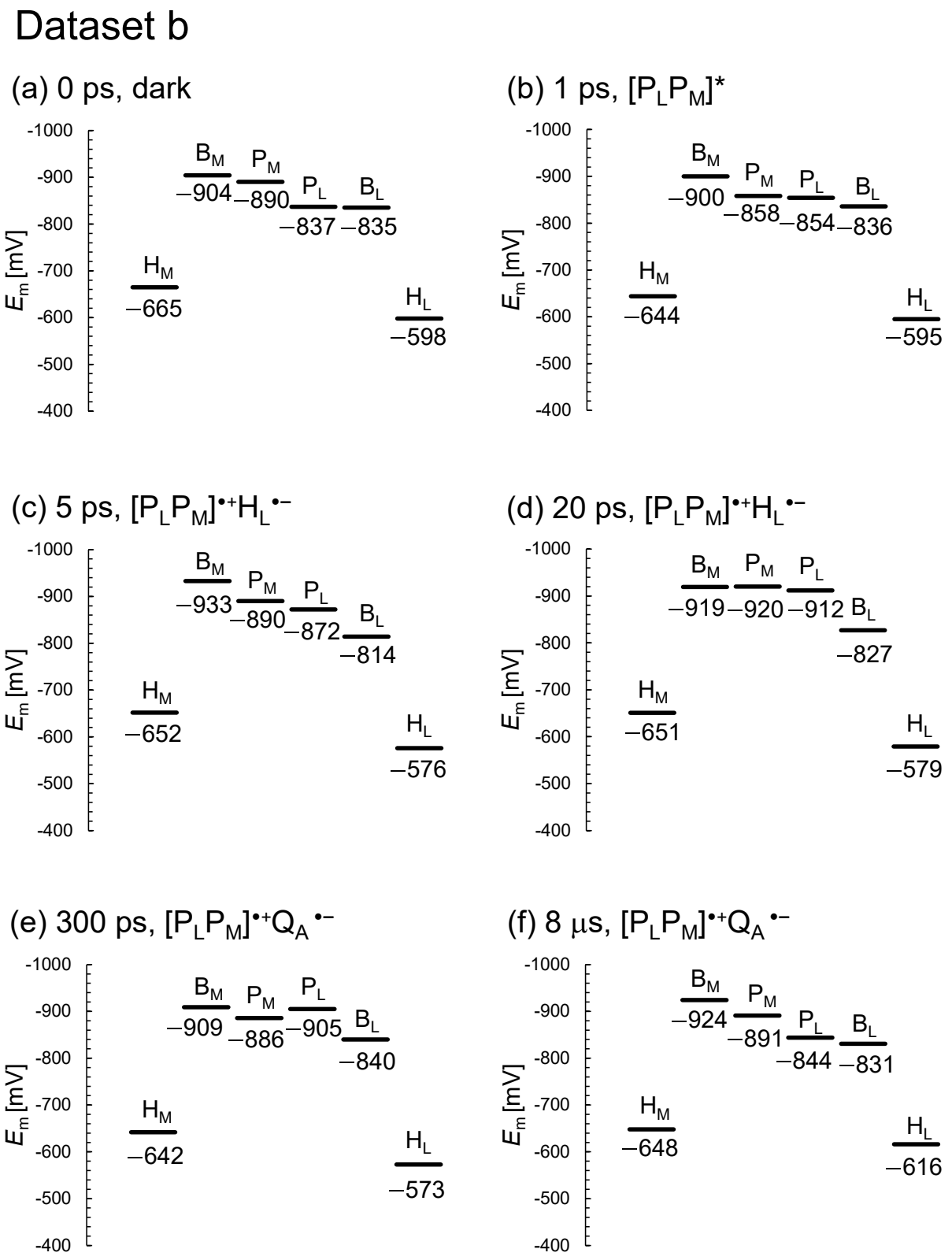

Figure 3. E_m profiles along the L- and M-branches in the XFEL structures for dataset b. (a) 0 ps. (b) 1 ps. (c) 5 ps. (d) 20 ps. (e) 300 ps. (f) 8 μs.

144

145

146 Among the L/M residue pairs, the Phe-L181/Tyr-M208 pair contributes to $E_m(B_L) > E_m(B_M)$ most
147 significantly (27 mV), facilitating L branch electron transfer, as suggested in theoretical studies (*25*)
148 (Table 1, Figure 3a). This result is also consistent with the contribution of the Phe-L181/Tyr-M210 pair
149 to the difference between $E_m(B_L)$ and $E_m(B_M)$, which was the largest in PbRC from *Rhodobacter*
150 *sphaeroides* (*26*) (26 mV (*13*)). The Asn-L158/Thr-M185 pair also contributes to the difference between
151 $E_m(B_L)$ and $E_m(B_M)$ (11 mV, Table 1), as does the Val-L157/Thr-M186 pair in PbRC from *Rhodobacter*
152 *sphaeroides* (22 mV (*13*)).

153

154 **Table 1**. Contributions of the L/M residue pairs that are responsible for $E_m(B_L) > E_m(B_M)$ (more than 10
155 mV) in the dark-state structure (mV). Difference: [contribution of subunit L to $E_m(B_L)$] + [contribution of
156 subunit M to $E_m(B_L)$] – [contribution of subunit L to $E_m(B_M)$] – [contribution of subunit M to $E_m(B_M)$].

Subunit L	$E_m(B_L)$	$E_m(B_M)$	**Subunit M**	$E_m(B_L)$	$E_m(B_M)$	**Difference**
Phe-L181	0	17	Tyr-M208	39	-3	25
His-L144	-8	-2	Glu-M171	-14	-45	25
Asn-L158	5	-6	Thr-M185	-3	-4	12

157

158 The E_m values for H_L are ~50 mV higher than those for H_M in the dark state and [5 ps and 300 ps]
159 XFEL structures, as observed in $E_m(B_L)$ and $E_m(B_M)$ (Figure 2a,c,e). However, the E_m difference decreases
160 to ~25 mV in the [1 ps, 20 ps, and 8 μs] XFEL structures (Figure 2b,d,f), which implies that the dark state
161 and [5 ps and 300 ps] XFEL structures are distinct from the [1 ps, 20 ps, and 8 μs] XFEL structures (see
162 below). Below, we discuss the dark state structure if not otherwise specified.

163 The Ala-L120/Asn-M147 pair contributes to $E_m(H_L) > E_m(H_M)$ most significantly (38 mV) (Table 2,
164 Figure S2). However, this holds true only for PbRC from *Blastochloris viridis*, as Asn-M147 is replaced

with alanine (Ala-M149) in PbRC from *Rhodobacter sphaeroides*. The Asp-L218/Trp-M252 pair decreases $E_m(H_M)$ with respect to $E_m(H_L)$, thereby contributing to $E_m(H_L) > E_m(H_M)$ (20 mV) (Table 2, Figure S2). Arg-L103 orients toward the protein interior, whereas Arg-M130 orients toward the protein exterior (Figure S2), which contributes to $E_m(H_L) > E_m(H_M)$ (17 mV) (Table 2). Ser-M271 forms an H-bond with Asn-M147 near H_M (Figure 3b). Thus, the contribution of Ser-M271 to $E_m(H_L)$ is large, although this residue is replaced with alanine (Ala-M273) in PbRC from *Rhodobacter sphaeroides*.

Table 2. Contributions of the L/M residue pairs that are responsible for $E_m(H_L) > E_m(H_M)$ (more than 10 mV) in the dark-state structure (mV). Difference: [contribution of subunit L to $E_m(H_L)$] + [contribution of subunit M to $E_m(H_L)$] – [contribution of subunit L to $E_m(H_M)$] – [contribution of subunit M to $E_m(H_M)$].

Subunit L	$E_m(H_L)$	$E_m(H_M)$	**Subunit M**	$E_m(H_L)$	$E_m(H_M)$	**Difference**
Ala-L120	-4	0	Asn-M147	0	-42	38
Asp-L218	-2	-22	Trp-M252	1	0	20
Arg-L103	77	3	Arg-M130	3	59	17
Ala-L237	-2	0	Ser-M271	3	-16	16
Lys-L110	17	2	Ala-M137	0	3	14
Val-L219	1	5	Thr-M253	17	1	11
His-L211	1	0	Arg-M245	14	4	11

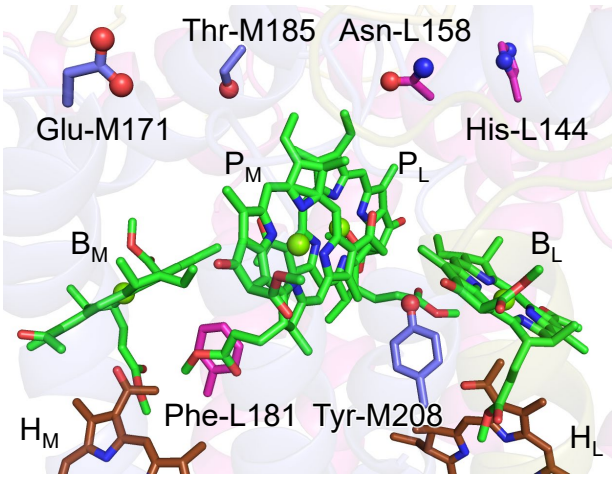

Figure 4. Residue pairs that are responsible for $E_m(B_L) > E_m(B_M)$.

178

179 **Relevance of structural changes observed in XFEL structures.** According to Dods et al., the 5-ps
180 and 20-ps structures correspond to the charge-separated $[P_LP_M]^{\bullet+}H_L^{\bullet-}$ state (*8*). If this is the case, $E_m(H_L)$
181 is expected to be exclusively higher in the 5-ps and 20-ps structures than in the other XFEL structures due
182 to the stabilization of the $[P_LP_M]^{\bullet+}H_L^{\bullet-}$ state by protein reorganization. In dataset a, the $E_m(H_L)$ value is
183 only 4 mV higher in the 5-ps structure than in the dark structure (Figure 5a). In dataset b, the $E_m(H_L)$ value
184 is ~20 mV higher in the 5- and 20-ps structures than in the dark structure (Figure 5b). However, the
185 $E_m(H_L)$ value is 25 mV higher in the 300-ps structure than in the dark structure. Tables 3 and 4 show the
186 residues that contribute to the slight increase in $E_m(H_L)$ most significantly in the 5- and 20-ps structures.
187 Most of these residues were in the region where Dods et al. specifically performed multiple rounds of
188 partial occupancy refinement (e.g., 153–178, 190, 230 and 236–248 of subunit L and 193–221, 232, 243–
189 253, 257–266 of subunit M) (*8*). In dataset b, which has more data points than dataset a, the contributions
190 of these residues to $E_m(H_L)$ often fluctuate (e.g., upshift/downshift followed by downshift/upshift) at
191 different time intervals (e.g., 1 to 5 ps, 5 to 20 ps, and 20 to 300 ps; Table 5). This result suggests that the
192 structural differences among the XFEL structures are not related to the actual time course of charge
193 separation. Furthermore, the $E_m(H_M)$ value in the inactive M branch is also ~15 mV higher in the 5- and
194 20-ps structures than in the dark structure (Figure 5b). These results suggest that the ~20 mV higher
195 $E_m(H_L)$ value in the 5- and 20-ps structures is not specifically due to the formation of the $[P_LP_M]^{\bullet+}H_L^{\bullet-}$
196 state. Thus, the stabilization of the $[P_LP_M]^{\bullet+}H_L^{\bullet-}$ state owing to protein reorganization is not clearly
197 observed in the $E_m(H_L)$ values.

198

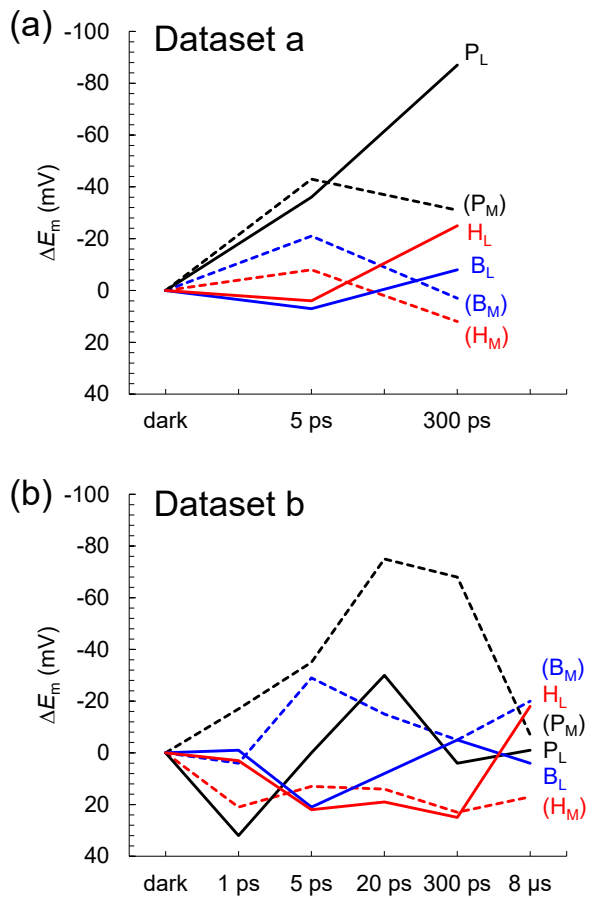

Figure 5. Time-dependent E_m changes for BChl*b* and BPheo*b* in the XFEL structures. (a) Dataset a. (b) Dataset b. ΔE_m denotes the E_m shift with respect to the dark state structure. Black solid lines: P_L; black dotted lines: P_M; blue solid lines B_L; blue dotted lines: B_M; red solid lines: H_L; red dotted lines: H_M.

Table 3. Residues that shift $E_m(H_L)$ most significantly during putative electron transfer in the XFEL structures (dataset a) (mV). The same residues are highlighted in the same colors for clarity.

Dataset a		**shift**		**shift**
0 to 5 ps	Ser-L176	5	Cys-M210	4
	Thr-M220	-7	B_L	-5
5 to 300 ps	B_L	7	Gly-M209	3
	Gly-M211	-11	Leu-M212	-8

207 **Table 4.** Residues that shift $E_m(H_L)$ most significantly during putative electron transfer in the XFEL

208 structures (dataset b) (mV). The same residues are highlighted in the same colors for clarity.

Dataset b		**shift**		**shift**
0 to 1 ps	Ser-L238	8	Ser-L176	7
	B_L	-7	Leu-M213	-3
1 to 5 ps	Gly-M211	6	Leu-M213	5
	Ser-L238	-6	Thr-M253	-5
5 to 20 ps	B_L	12	Thr-M253	7
	Leu-M213	-4	P_M	-3
20 to 300 ps	Ser-L238	3	Gly-M211	2
	B_L	-10	Glu-L212	-4
300 ps to 8 μs	Glu-L212	4	Leu-M213	4
	B_L	-6	Gly-M211	-5

209

210 A normal-coordinate structural decomposition (NSD) analysis (*9, 10*) of the out-of-plane distortion of

211 the chlorin ring is sensitive to subtle structural changes in the chlorin ring, which are not distinct in the

212 E_m changes (*6*). QM/MM calculations indicate that $H_L^{\bullet-}$ formation induces the saddling mode in the

213 chlorin ring, which describes the movement of rings I and III being in the opposite direction to the

214 movement of rings II and IV along the normal axis of the chlorin ring (Table 5). However, (i) in the XFEL

215 structures, the saddling mode of H_L remains practically unchanged in dataset a during electron transfer

216 (Figure 6 and Tables S2 and S3). In dataset b, the saddling mode of H_L is induced most significantly at 1

217 ps, which does not correspond to the charge-separated $[P_LP_M]^{\bullet+}H_L^{\bullet-}$ state (Figure 7). (ii) In addition, the

218 ruffling mode is more pronounced than the saddling mode in H_L (Figure 7), which suggests that the

219 observed deformation of H_L is not directly associated with the reduction of H_L.

220

Table 5. Induced out-of-plane distortion of H_L and H_M in the PbRC protein environment of the dark structure for dataset a in response to the reduction (Å).

	saddling	ruffling	doming	waving		propellering
	B_{2u}	B_{1u}	A_{2u}	$E_{g(x)}$	$E_{g(y)}$	A_{1u}
H_L	0.18	0.35	-0.10	0.13	-0.11	0.13
$H_L^{\bullet-}$	0.24	0.35	-0.09	0.12	-0.12	0.13
difference	0.06	0.00	0.01	-0.01	-0.01	0.00
H_M	0.06	0.40	-0.20	0.37	0.12	0.19
$H_M^{\bullet-}$	0.12	0.38	-0.22	0.33	0.09	0.22
difference	0.06	-0.02	-0.02	-0.04	-0.03	0.03

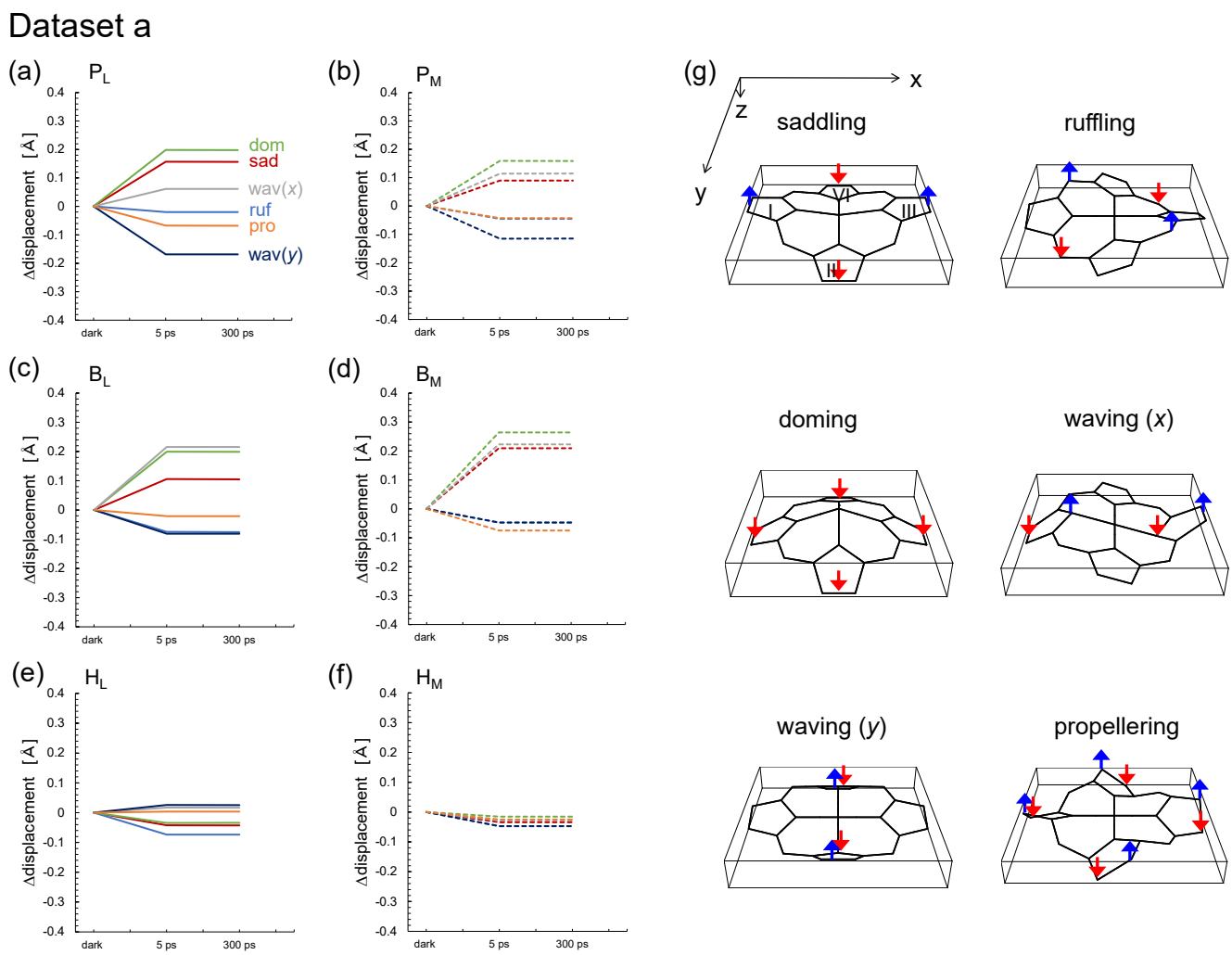

Figure 6. Time-dependent changes in the lowest frequency out-of-plane modes of the chlorin rings in the XFEL structures (dataset a). Sad: saddling (red); ruf: ruffling (blue); dom: doming (green); wav(x, y): waving (x, y) (gray, dark blue); pro: propellering (orange). Solid and dotted lines indicate L and M branches, respectively. See Table S2 for the absolute values in the dark state for dataset a.

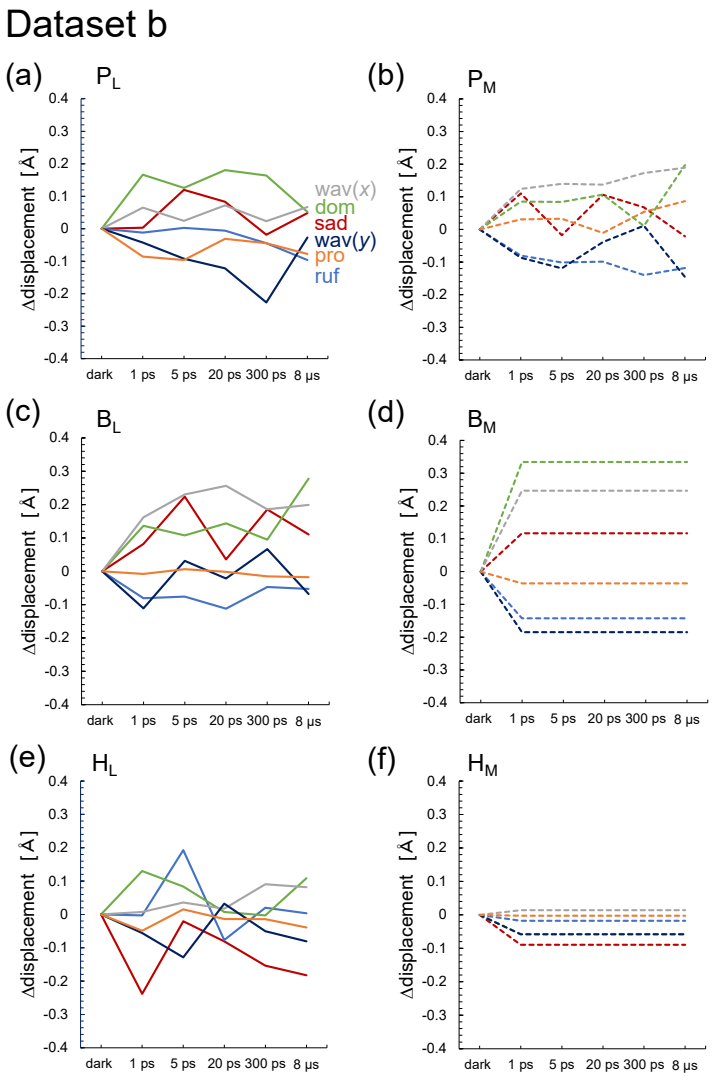

Figure 7. Time-dependent changes in the lowest frequency out-of-plane modes of the chlorin rings in the XFEL structures (dataset b). Sad: saddling (red); ruf: ruffling (blue); dom: doming (green); wav(x, y): waving (x, y) (gray, dark blue); pro: propellering (orange). Solid and dotted lines indicate L and M branches, respectively. See Table S3 for the absolute values in the dark state for dataset b.

235

236 In summary, the E_m values in the active L branch are higher than those in the inactive M branch in the
237 XFEL structures, which suggests that electron transfer via $B_L^{\bullet-}$ and $H_L^{\bullet-}$ is energetically more favored
238 than that via $B_M^{\bullet-}$ and $H_M^{\bullet-}$ (Figure 2). The Phe-L181/Tyr-M208 pair contributes to the difference between
239 $E_m(B_L)$ and $E_m(B_M)$ the most significantly, as observed in the Phe-L181/Tyr-M210 pair in PbRC from
240 *Rhodobacter sphaeroides* (*13, 26*). The stabilization of the $[P_LP_M]^{\bullet+}H_L^{\bullet-}$ state owing to protein
241 reorganization is not clearly observed in the $E_m(H_L)$ values (Figure 5). The absence of the induced
242 saddling mode in the H_L chlorin ring in the 5- and 20-ps structures suggests that $H_L^{\bullet-}$ does not specifically
243 exist in these XFEL structures (Figures 6 and 7). The cyclic fluctuations in the contributions of the
244 residues to $E_m(H_L)$ at different time intervals suggest that the structural differences among the XFEL
245 structures are not related to the actual time course of charge separation (Table 4). The major problem of
246 the structural studies by Dods et al. (*8*) is that their XFEL structures are mostly at a resolution of 2.8 Å.
247 Changes in E_m and chlorin ring deformations identified using the XFEL structures therefore may reflect
248 the experimental errors rather than the real structural changes induced by the electron transfer events.
249 Therefore, the time-dependent structural changes proposed by Dods et al. (*8*) are highly likely irrelevant
250 to the electron transfer events. Future high-resolution structures may provide further insights into the
251 actual structural changes relevant to electron transfer events.

252

253 **ACKNOWLEDGMENTS**

254 This research was supported by JSPS KAKENHI (JP23H04963 to K.S.; JP20H03217 and JP23H02444
255 to H.I.) and Interdisciplinary Computational Science Program in CCS, University of Tsukuba.

256

257 **Competing financial interests**

258 The authors declare no financial and non-financial competing interests.

REFERENCES

1. Deisenhofer, J.; Epp, O.; Miki, K.; Huber, R.; Michel, H. (1985) Structure of the protein subunits in the photosynthetic reaction centre of *Rhodopseudomonas viridis* at 3 Å resolution, *Nature 318*, 618-624.
2. Rabenstein, B.; Ullmann, G. M.; Knapp, E.-W. (1998) Energetics of electron-transfer and protonation reactions of the quinones in the photosynthetic reaction center of *Rhodopseudomonas viridis*, *Biochemistry 37*, 2488-2495.
3. Kirmaier, C.; Laible, P. D.; Hanson, D. K.; Holten, D. (2003) B-side charge separation in bacterial photosynthetic reaction centers: nanosecond time scale electron transfer from H_B^- to Q_B, *Biochemistry 42*, 2016-2024.
4. Holzapfel, W.; Finkele, U.; Kaiser, W.; Oesterhelt, D.; Scheer, H.; Stilz, H. U.; Zinth, W. (1990) Initial electron-transfer in the reaction center from *Rhodobacter sphaeroides*, *Proc Natl Acad Sci U S A 87*, 5168-5172.
5. Marcus, R. A.; Sutin, N. (1985) Electron transfers in chemistry and biology, *Biochim. Biophys. Acta 811*, 265-322.
6. Saito, K.; Umena, Y.; Kawakami, K.; Shen, J. R.; Kamiya, N.; Ishikita, H. (2012) Deformation of chlorin rings in the photosystem II crystal structure, *Biochemistry 51*, 4290-4299.
7. Müh, F.; Williams, J. C.; Allen, J. P.; Lubitz, W. (1998) A conformational change of the photoactive bacteriopheophytin in reaction centers from *Rhodobacter sphaeroides*, *Biochemistry 37*, 13066-13074.
8. Dods, R.; Båth, P.; Morozov, D.; Gagnér, V. A.; Arnlund, D.; Luk, H. L.; Kübel, J.; Maj, M.; Vallejos, A.; Wickstrand, C.; Bosman, R.; Beyerlein, K. R.; Nelson, G.; Liang, M.; Milathianaki, D.; Robinson, J.; Harimoorthy, R.; Berntsen, P.; Malmerberg, E.; Johansson, L.; Andersson, R.; Carbajo, S.; Claesson, E.; Conrad, C. E.; Dahl, P.; Hammarin, G.; Hunter, M. S.; Li, C.; Lisova, S.; Royant, A.; Safari, C.; Sharma, A.; Williams, G. J.; Yefanov, O.; Westenhoff, S.; Davidsson, J.; DePonte, D. P.; Boutet, S.; Barty, A.; Katona, G.; Groenhof, G.; Brändén, G.; Neutze, R. (2021) Ultrafast structural changes within a photosynthetic reaction centre, *Nature 589*, 310-314.
9. Jentzen, W.; Song, X.-Z.; Shelnutt, J. A. (1997) Structural characterization of synthetic and protein-bound porphyrins in terms of the lowest-frequency normal coordinates of the macrocycle, *J Phys Chem B 101*, 1684-1699.
10. Shelnutt, J. A.; Song, X.-Z.; Ma, J.-G.; Jia, S.-L.; Jentzen, W.; Medforth, C. J. (1998) Nonplanar porphyrins and their significance in proteins, *Chem Soc Rev 27*, 31-41.
11. Brooks, B. R.; Bruccoleri, R. E.; Olafson, B. D.; States, D. J.; Swaminathan, S.; Karplus, M. (1983) CHARMM: a program for macromolecular energy minimization and dynamics calculations, *J. Comput. Chem. 4*, 187-217.
12. MacKerell, A. D., Jr.; Bashford, D.; Bellott, R. L.; Dunbrack, R. L., Jr.; Evanseck, J. D.; Field, M. J.; Fischer, S.; Gao, J.; Guo, H.; Ha, S.; Joseph-McCarthy, D.; Kuchnir, L.; Kuczera, K.; Lau, F. T. K.; Mattos, C.; Michnick, S.; Ngo, T.; Nguyen, D. T.; Prodhom, B.; Reiher, W. E., III; Roux, B.; Schlenkrich, M.; Smith, J. C.; Stote, R.; Straub, J.; Watanabe, M.; Wiorkiewicz-Kuczera, J.; Yin, D.; Karplus, M. (1998) All-atom empirical potential for molecular modeling and dynamics studies of proteins, *J. Phys. Chem. B 102*, 3586-3616.
13. Kawashima, K.; Ishikita, H. (2018) Energetic insights into two electron transfer pathways in light-driven energy-converting enzymes, *Chem Sci 9*, 4083-4092.
14. Kawashima, K.; Ishikita, H. (2017) Structural factors that alter the redox potential of quinones in cyanobacterial and plant photosystem I, *Biochemistry 56*, 3019-3028.

15. Bayly, C. I.; Cieplak, P.; Cornell, W. D.; Kollman, P. A. (1993) A well-behaved electrostatic potential based method using charge restraints for deriving atomic charges: the RESP model, *J. Phys. Chem. 97*, 10269-10280.
16. Jaguar. (2012), version 7.9, Schrödinger, LLC, New York, NY.
17. Bashford, D.; Karplus, M. (1990) Pkas of Ionizable Groups in Proteins - Atomic Detail from a Continuum Electrostatic Model, *Biochemistry 29*, 10219-10225.
18. Fajer, J.; Davis, M. S.; Brune, D. C.; Spaulding, L. D.; Borg, D. C.; Forman, A. (1976) Chlorophyll radicals and primary events, *Brookhaven Symp. Biol. 28*, 74.
19. Watanabe, T.; Kobayashi, M. (1991) Electrochemistry of chlorophylls, *in Chlorophylls (Scheer, H., Ed.)*, pp 287-303, CRC Press, Boca Raton, FL.
20. Rabenstein, B.; Knapp, E. W. (2001) Calculated pH-dependent population and protonation of carbon-monoxy-myoglobin conformers, *Biophys. J. 80*, 1141-1150.
21. QSite. (2012), version 5.8, Schrödinger, LLC, New York, NY.
22. Zucchelli, G.; Brogioli, D.; Casazza, A. P.; Garlaschi, F. M.; Jennings, R. C. (2007) Chlorophyll ring deformation modulates Qy electronic energy in chlorophyll-protein complexes and generates spectral forms, *Biophys J 93*, 2240-2254.
23. Tamura, H.; Saito, K.; Ishikita, H. (2020) Acquirement of water-splitting ability and alteration of the charge-separation mechanism in photosynthetic reaction centers, *Proc Natl Acad Sci U S A 117*, 16373-16382.
24. Rutherford, A. W.; Heathcote, P.; Evans, M. C. W. (1979) Electron-paramagnetic-resonance measurements of the electron-transfer components of the reaction centre of *Rhodopseudomonas viridis*. Oxidation–reduction potentials and interactions of the electron acceptors, *Biochemical Journal 182*, 515-523.
25. Gunner, M. R.; Nicholls, A.; Honig, B. (1996) Electrostatic potentials in *Rhodopseudomonas viridis* reaction centers: implications for the driving force and directionality of electron transfer, *J. Phys. Chem. 100*, 4277-4291.
26. Parson, W. W.; Chu, Z.-T.; Warshel, A. (1990) Electrostatic control of charge separation in bacterial photosynthesis, *Biochim. Biophys. Acta 1017*, 251-272.